Feasibility Study on Acquisition, Tracking, and Pointing Using Earth Thermal Images for Deep-Space Ka-Band and Optical Communications

S. Lee,[1] G. G. Ortiz,[1] W. T. Roberts,[1] and J. W. Alexander[2]

The feasibility of using long-wavelength Earth thermal (infrared) images for antenna/telescope tracking/pointing applications for both deep-space Ka-band (18 to 35 GHz) and free-space optical communications has been investigated and is reported on here. The advantage of this technology rests on using full Earth images in this band that yield more accurate estimates of geometric centroids than those of Earth images in the visible band. Furthermore, these images are nearly independent of Earth phase angle. The results of the study show that, at a Mars range with currently available sensors, a noise equivalent angle of 10 to 150 nrad and a bias error of better than 80 nrad can be obtained. This would enable precise pointing of both the optical and Ka-band communications beams.

I. Introduction

The use of Earth image tracking in the visible band to accurately point the optical communication downlink signal beam to receiver telescopes on the Earth has been investigated for more than a decade [2,3,6]. The major limitations with this concept have been (a) a low signal level at high Earth phase angles and (b) a large albedo variation due to Earth atmospheric changes [4]. Use of Earth tracking in the thermal band significantly mitigates the above problem. With thermal imaging, a full Earth image can be maintained even for high phase angles. Low emissivity variations of thermal images are shown; this is due to the relatively slow thermal changes of the Earth surfaces compared with rapid changes of reflectivity of the Earth surface for the visible wavelength. The recent release from the Mars Odyssey program shows that the entire (full) Earth thermal image was successfully taken, whereas the visible-light image shows the thin crescent Earth viewed from Odyssey's perspective (Fig. 1). These images, taken at a distance of 3,563,735 km on April 19, 2001, as the Mars Odyssey spacecraft left Earth, support the potential of Earth thermal images in tracking/pointing applications.

---

[1] Communications Systems and Research Section.
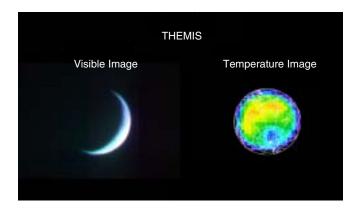
[2] Autonomy and Control Section.

Fig. 1. Visible Earth image versus thermal image.

The effort has focused on validation of the tracking/pointing accuracy using the measured Earth thermal images and emissivity variations. For the wide range of emissivity variations, simulations have been used to estimate the impact to the centroid accuracy. Investigation of available infrared detectors has been made to assess the readiness of the detector technology. The estimated pointing accuracy has been compared with the required pointing accuracy for various scenarios of Ka-band (18 to 35 GHz) and optical communications.

II. Description of Concept

The basic concept is to use a long-wavelength infrared (LWIR) sensor to collect images of the Earth. The Earth image serves as the reference to the communications tracking and pointing system. Tracking on the Earth closes the pointing loop in this "beacon-less" approach. The location of the Earth receiver is determined by (a) computing the Earth's centroid location from the image and (b) calculating the receiver location relative to the center of the Earth based on time information and an onboard model. Any error in this determination is known as the bias error.

III. Technical Approach

In order to determine if Earth's LWIR images can be used for pointing the communications beam, the tracking errors need to be estimated and compared with the required performance.

A. Requirements

The tracking error is mainly composed of two terms: the random error, or noise equivalent error (NEA), and the bias error. The required performance has been obtained for a Mars mission for both optical (Table 1) and Ka-band communications (Table 2): an NEA of 300 nrad and 35 μrad and a bias error of 100 nrad and 10 μrad for optical and Ka-band, respectively. Ka-band requirements were obtained from the 0.1-dB pointing loss (equivalent to the current X-band (7 to 8.5 GHz) pointing loss) with approximate allocations to the various error sources.

B. Random Error Estimate

Random error, or noise equivalent error, is mainly governed by the signal-to-noise ratio (SNR). Therefore, accurate estimation of the total signal at the detector and of the system noise is critical. The steps taken here for NEA estimation are selection of the wavelength, estimation of the available signal, estimation of the background noise, and determination of the LWIR detector characteristics. The first two steps

Table 1. Requirements for an optical communications link [1].

Parameter	Value	Rationale
Noise equivalent angle	300 nrad	For a Mars high-rate link, the total jitter budget is 500 nrad. This is the allocation to the reference "beacon" NEA. It includes the effects of centroid window size, pixel field of view, total signal on centroid area, read noise, dark current, integration time, full well, and analog-to-digital converter (ADC) effective resolution.
Centroid bias error	100 nrad	For a Mars high-rate link, the total bias budget is 500 nrad. This is the allocation to the centroid bias error. It is mainly affected by emissivity variations from Earth's thermal emission and the error in modeling them accurately.
Sensor update rate	10–1000 Hz	A sensor with an update rate in this range is sufficient. For low rates, inertial sensors, angle sensors, and gyros are used to compensate for high-frequency spacecraft micro-vibrations. With high sampling sensors, including integration time, the micro-vibration compensation can be done directly.

Table 2. Requirements for a Ka-band communications link.

Parameter	Value	Rationale
Sensor noise equivalent angle	35 μrad (0.002 deg)	To provide a 0.1-dB loss in the effective isotropic radiated power (EIRP) from the peak of the beam, an overall pointing accuracy of 20 mdeg (350 μrad) is needed. This is the allocation to the sensor NEA.
Centroid bias error	10 μrad	To provide a 0.1-dB loss in the EIRP from the peak of the beam, an overall pointing accuracy of 20 mdeg (350 μrad) is needed. This is the allocation to the centroid bias error.
Sensor update rate, coarse tracking	1–10 Hz	A sensor with an update rate in this range is sufficient. This sensor is primarily used for coarse pointing.
Sensor update rate, fine tracking	10–100 Hz	In order to provide feedback of Earth's position to do fine tracking, the update rate is increased to compensate for propagated spacecraft micro-vibrations.

provide an estimation of the signal, and the last two steps address the noise level. The desired wavelength band should maximize SNR (to get a low NEA) and minimize the emissivity variation for various phase angles (to lower bias error). For the wavelength band selection, the wavelength band from 3 to 13 μm is divided into several bands, and then signal strength and emissivity variations are investigated. Once a certain wavelength band is determined, the available signal level can be estimated. Major background noise sources include solar stray light, while the effect of some other noise sources, such as emissions from city lights and the atmosphere, may need to be investigated. Detector noise is largely dependent upon specific detector material and manufacturing process/design. The objective of trade-offs among these parameters is to maximize the SNR, thus minimizing the NEA.

1. Wavelength Selection. The advantage of using LWIR Earth images is the ability of the Earth-tracking sensor to observe energy emission from the Earth rather than reflected solar energy. The optimum spectral band involves a trade-off between the need for more signals to overcome the detector noise and the pointing bias introduced by thermal variations across the Earth's surface.

As Fig. 2 indicates, the spectral signal variations for blackbodies of different temperatures vary much more at the shorter wavelengths, so we preferentially select the longer wavelengths to minimize any bias
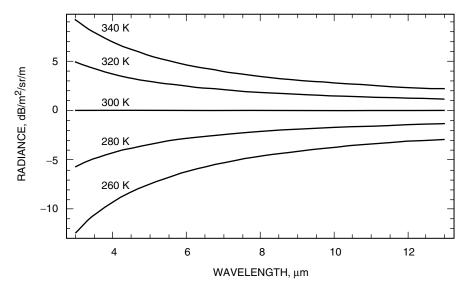
Fig. 2. Spectral signal versus wavelength: spectral signal variations for blackbodies of different temperatures vary much more at the shorter wavelengths.

error resulting from this effect. Additional advantage in the use of longer-wavelength radiation is attained from the reduction of direct solar background and solar scattering from the Earth's surface.

The ability of the LWIR tracking system to generate an accurate Earth centroid value is related to the signal-to-noise ratio in the sensor used to image the Earth. If the noise level on each pixel is not much lower than the signal value, the effect will be a skewing of the final centroid value from the true value. Several different types of noise exist in detectors, and the amount of each varies from detector to detector. The aggregate noise on detectors tends to grow more slowly with integration time than does the accumulated signal, affording some potential to improve the signal-to-noise ratio by operating the sensor at lower speeds, but this approach reduces the Earth centroid update rate.

The approach for selecting a spectral band is to start at the 13-μm end of the 8- to 13-μm waveband and integrate the signal down to the spectral point at which the improvement to centroid estimation from higher signal-to-noise ratios is offset by the centroid skewing inherent in the use of shorter wavelengths. The rationale for using the 8- to 13-μm waveband is its high atmospheric transmission [5] and higher blackbody radiation (Fig. 3). The available radiance for this approach is shown in Fig. 3. The roll-off of the curve at shorter wavelengths further demonstrates the lack of value in extending the spectral band to shorter and shorter wavelengths. At shorter wavelengths, the variation of the radiance is larger over the entire phase angle (Fig. 4). This radiance variation directly affects centroid skewing.

Based on this result, we have chosen three spectral bands for comparison. The 3- to 5-μm transmission window of Earth was evaluated and appears to be a rather poor choice. Only a very small fraction of the thermal energy is emitted in this band, and because of the short wavelengths, that means even fewer photons. Additionally, consideration of the blackbody curves in Fig. 3 shows that the background from scattered solar radiation will be much, much higher than would be found around 10 μm. Finally, since Rayleigh photon scattering is proportional to λ^{-3}, there will be over 20 times more Rayleigh background in the 3- to 5-μm band than around 10 μm.

The 10- to 13-μm band looks quite good. There is a strong signal integrated over a full 3-μm band. Increasing the width of the band to 8 to 13 μm increases the signal strength by about 2 dB, according to this model. However, the model doesn't take into account the strong atmospheric absorption of the CO_2 band that reduces the signal gain rather significantly. Also, there is more diurnal variation in the
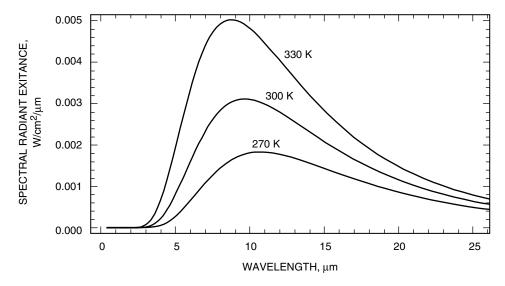
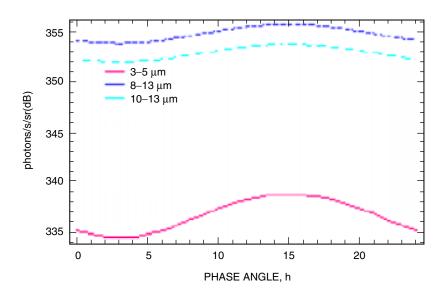**Fig. 3. Spectral radiance as a function of wavelength for three temperatures: 270 K, 300 K, and 330 K.**

Fig. 4. Spectral signal for three wavelength bands.

8- to 13-μm signal and, consequently, more spectral skewing of the Earth centroid. Finally, for the 8- to 10-μm waveband, there is about 25 percent more solar-induced background than there is in the 10- to 13-μm waveband, resulting in much more reduction in the background level than in the signal level by limiting the band.

2. Estimated Available Signal Level. We have generated a computer model to estimate the effects of thermal variations across the surface of the Earth. The model calculates a very crude surface temperature profile based on expected diurnal, seasonal, and latitudinal variations. The model generates smoothly varying temperature profiles, without the steep gradients expected from weather patterns or surface topography. To obtain an available signal level, the model integrates the spectral radiance in the specified waveband for a selection of spatial points across the visible Earth surface. By multiplying by the known area of the Earth's surface, we obtain the radiant intensity of the Earth (photons/s/sr). For the rest of the article, we select the 8- to 13-μm band as the most promising waveband for our concept.

Since the temperature of the visible portion of the Earth varies by season and by aspect angle (Sun–Earth–probe (SEP) angle), we plot these values in Fig. 5 as a function of hour (of local time) and for solstice versus equinox.

3. Background Noise Level. The majority of available LWIR detector arrays are designed for background-limited operation in a high-background Earth-based environment. However, our mission is space-based and, as such, can expect that much lower background levels will result. This means that there will be much less background noise, so the sensitivity of the array can be considerably higher than the quoted values, depending upon how much better than the "background limit" the preamplifier noise level of the detector is.

The actual LWIR background available will come from three sources: stars in the background field, thermal emission in the telescope, and solar light scattered from optical surfaces in the telescope. The number of stars per square degree at various spectral irradiance levels at an 11-μm wavelength is presented in [5, pp. 3–30]. Based on a 10-mrad square field of view (FOV), we can anticipate that at any point the camera will see a power density per unit wavelength consisting of 3,000 to 30,000 sources emitting 10^{-20} W/cm^2/μm, 300 to 3,500 sources emitting 10^{-19} W/cm^2/μm, 30 to 350 sources emitting 10^{-18} W/cm^2/μm, 2 to 25 sources emitting 10^{-17} W/cm^2/μm, 0.1 to 0.2 sources emitting 10^{-16} W/cm^2/μm, and 0.004 to 0.005 sources emitting 10^{-15} W/cm^2/μm. By comparison, the spectral irradiance from the Earth at maximum distance is 6×10^{-13} W/cm^2/μm, roughly three orders of magnitude larger than the other sources.

Radiation from non-optical surfaces in the telescope (struts, baffles, spiders, etc.) has the potential to act as a very high-level background source at these wavelengths. For this reason, these sources generally are masked out of the system by placing the low-temperature detector in a cold enclosure and limiting the radiation from out-of-field sources in the warm, front part of the telescope with a cold stop. This is standard practice and has been proven quite effective at limiting the direct internal emission of background light.

The final background source to consider is solar light scattered from optical surfaces (typically the primary mirror) within the telescope. As the Earth approaches its transit of the Sun, the communication terminal must point closer and closer to the Sun. At some point the Sun will illuminate the primary mirror of the terminal telescope. Even though the Sun is outside the field of view of the detector array, the primary mirror will scatter some fraction of that light into the field of view and increase the background on the detector. This probably will not be as significant a source as it would seem at first; less than
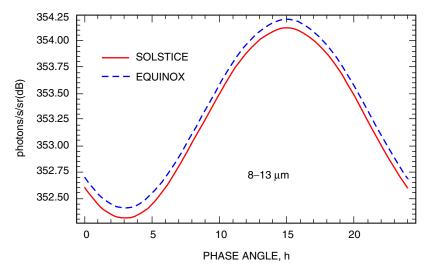

Fig. 5. Earth thermal signal level for solstice versus equinox.

0.1 percent of the Sun's energy is emitted in the 8- to 13-μm band, and the scattering coefficients are over three orders of magnitude lower at these wavelengths than in the visible. We must assume a scatter level for the mirror [5, pp. 7–79], and assuming a Rayleigh spectral scattering dependence (i.e., $\sim 1/\lambda^3$), we calculate that the 10-μm scattering coefficient at 1 deg off axis is 3×10^{-5}/sr. At the distance of Mars, the solar spectral irradiance at 10 μm is roughly 0.1 W/m^2/μm, for a total of 0.007 W/μm incident on a 30-cm-diameter aperture. If a single detector subtends 10×10 μrad (10^{-10} sr), then the amount of scatter incident on a single detector under full solar illumination of the primary mirror would be about 2×10^{-17} W/μm. Thus, it too is relatively insignificant.

4. Noise Equivalent Angle Estimate. The photon radiant intensity values in Fig. 4, with the assumed parameter values in Table 3, were used to estimate the NEA. For simplicity, the center of brightness centroid is discussed here. Since the Earth image is a relatively uniform disk, we assume that each pixel in the sum experiences the same noise due to sensor plus signal photon statistics. All quantities are assumed to be measured in electrons. DT is the integration time used for dark current noise, and DC is the dark current rate in electrons/second. The basic center-of-brightness centroiding formula for a uniform signal (pixel value $D_{i,j}$ after background compensation) with a variance formula (assuming very large total signal, T, to take it outside the expectation) given by variance S_x (S_y is similarly computed) is approximately given by

$$\left. \begin{aligned} T &= \sum_{j=1}^{M}\sum_{i=1}^{N} D_{i,j} \\[12pt] S_x &= \sum_{j=1}^{M}\sum_{i=1}^{N} i \times D_{i,j} \\[12pt] S_y &= \sum_{j=1}^{M}\sum_{i=1}^{N} j \times D_{i,j} \end{aligned} \right\} \tag{1a}$$

Then

$$\left. \begin{aligned} x_c &= \frac{S_x}{T} \\[12pt] y_c &= \frac{S_y}{T} \end{aligned} \right\} \tag{1b}$$

$$\left. \begin{aligned} \text{Var}(S_x) &= \frac{N}{2} \times \frac{N/2 + 1}{3} \times \frac{T + N \times M \times \left(\text{Var(Read Noise } e) + DT(DC\,e)\right)}{T^2} \\[12pt] \text{Var}(S_y) &= \frac{M}{2} \times \frac{M/2 + 1}{3} \times \frac{T + N \times M \times \left(\text{Var(Read Noise } e) + DT(DC\,e)\right)}{T^2} \end{aligned} \right\} \tag{2}$$

Assuming $N = M$, and that the dark current noise is negligible, the variance simplifies to

$$\frac{N}{2} \times \frac{N/2 + 1}{3} \times \frac{T + N^2\left(\text{Var(Read Noise } e)\right)}{T^2} \tag{3}$$

Table 3. Assumptions for NEA estimations.[a]

Parameter	Value	Rationale
Centroid window size	9×9 pixels to <u>25×25 pixels</u>	Earth image of 60–220 μrad, 10 μrad/pixel, extra 3 pixels
Focal plane array (FPA) full well	20×10^6 to <u>30×10^6 electrons</u>	Specification of DRS Technologies IR FPA of 25- to 40-μm pixels
ADC effective bits	14 bits	14 bits
System noise (1 sigma)	200 electrons	Read noise+ electronic noise + background noise
Frame update rate	10 Hz to <u>1 kHz</u>	10 Hz (inertial sensor assisted) to <u>1 kHz (optical only)</u>
Aperture size	<u>10 cm</u> to 30 cm	Previous baseline for optical communication for deep space
Range	0.5 AU to <u>2.7 AU</u>	0.5 AU to <u>2.7 AU</u> (Mars missions)
Optical transmission efficiency + detector QE	10%	Detector QE of 80% and optical transmission of 13%

[a] Underlined values were used for the simulations presented in Figs. 6 and 7 (worst-case scenario).

There are two classes of parameters: one consists of design values such as aperture size and detector full well; the other is mission-dependent parameters such as range and centroid window size (governed by beacon spot size). Consider the two tracking scenarios, optical-only tracking and inertial-sensor-assisted tracking. The beacon update rates of 10 and 1 kHz were used, respectively. For inertial-sensor-assisted tracking, the NEA is very small—on the order of 10 nrad (10 μrad/pixel) for 8- to 13-μm bands (Fig. 6). For the 3- to 5-μm band, the NEA is up to 1 μrad, and with trade-offs on the detector full well and aperture size, this can be reduced to 70 nrad. For optical tracking only, the worst-case estimate of the NEA is more than 1 μrad. However, an NEA of better than 100 nrad can be achieved with the trade-offs on the smaller detector full well and larger aperture size (Fig. 7).

In summary, the bands of 8 to 13 μm and 10 to 13 μm can provide an adequate centroiding NEA for optical communication in both optical-only and inertial-sensor-assisted tracking with some trade-offs. However, the 3- to 5-μm band is not suitable for optical communication tracking, while it meets the Ka-band pointing requirements for NEA.

C. Bias Error Estimate

As with any optical communication tracking system, there are a few basic questions about the images that are to be tracked. The main questions to be answered are

(1) The amount of signal from the image—total flux

(2) The amount of stray signal (e.g., sunlight or moon in the case of Earth tracking, which introduce both additional photon noise and biases)

(3) How the image relates to the receiving station location (e.g., after computing the centroid of the Earth, how to use the centroid to determine the receiver location)

(4) Variability of the image measurement (this includes the choice of technique) and the predictability of that variability (e.g., albedo effects)

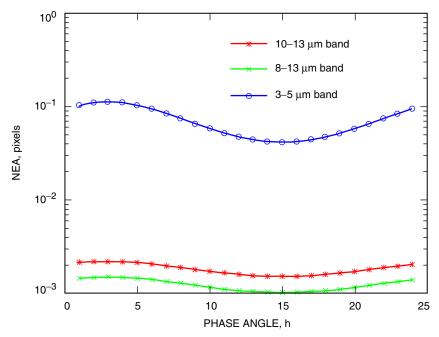(5) Techniques used to make the measurements

Fig. 6. NEA for inertial-sensor-assisted tracking update rate (10 Hz) using the worst-case scenario in Table 3.
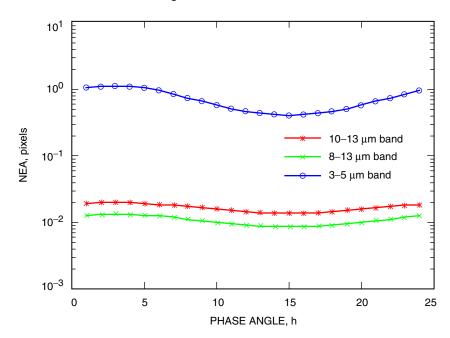

Fig. 7. NEA for optical tracking update rate (1 kHz) using the worst-case scenario in Table 3, except for the detector full well and aperture size.

It is expected that the bias error depends more on the knowledge of the Earth model than on the particular approach (there are different techniques under each approach). The work is in a very preliminary stage at this point. To start the process of answering some of the above questions, a series of LWIR images was generated using an Earth model as seen from different phase angles, as represented by the different cases (details of the different cases are listed in Table 4). The procedure for the Earth temperature model is described in the appendix. The centroids are computed based on the image distribution model (taken at the highest resolution of the data, 205×205). The "% shift" in Table 5 gives the comparison of the geometric centroid (each pixel equally weighted, representing the outline of the body) and the center of brightness. The differences between the different cases show the need to calibrate the

Table 4. Signal, phase angle, SNR, etc., for various cases, at 5–6 μm and at 10–11 μm.

Case[a,b]	Signal, J	Phase angle, deg	Earth–Mars distance, AU	Waveband mid-point (1-μm width)	(10 to 11)/(5 to 6) photon ratio	Estimated photo-electrons/μm, 10% at kHz	Normalized to 1 AU (reference only), 10% at kHz	Ka-band maximum pixel count at 20:1 SNR	Optical maximum pixel count at 100:1 SNR
1(a)	9.15×10^{-11}	16	2.5	5.5	—	253,278	1,582,988	60	10
1(b)	3.32×10^{-10}	16	2.5	10.5	6.926	1,754,120	10,963,249	417	68
2(a)	8.14×10^{-10}	94	1.15	5.5	—	2,253,290	2,979,977	536	88
2(b)	2.15×10^{-9}	94	1.15	10.5	5.037	11,348,874	15,008,885	2,699	443
3(a)	3.85×10^{-10}	172	0.67	5.5	—	1,066,486	478,745	254	42
3(b)	1.25×10^{-9}	172	0.67	10.5	6.210	6,622,787	2,972,969	1,575	259
4(a)	1.53×10^{-9}	90	1.32	5.5	—	4,232,097	7,374,006	1,006	165
4(b)	4.89×10^{-9}	90	1.32	10.5	6.108	25,848,021	45,037,591	6,147	1,009

[a] The band from 5 to 6 μm is denoted by (a).

[b] The band from 10 to 11 μm is denoted by (b).

Table 5. The "% shift" gives the comparison of the geometric centroid (each pixel equally weighted, representing the outline of the body) and the center of brightness.

Case	Waveband		% shift compared to geometric centroid	
	Start, μm	Width, μm	East–West	North–South
1(a)	5	1	−5.06	1.23
1(b)	10	1	−2.54	0.79
2(a)	5	1	−4.93	−0.53
2(b)	10	1	−2.66	−0.33
3(a)	5	1	−6.06	−4.1
3(b)	10	1	−3.09	−2.62
4(a)	5	1	6.11	0.36
4(b)	10	1	3.1	0.23

image distribution. The difference within a single case—e.g., between the 5- to 6-μm and 10- to 11-μm case—shows that knowledge of the relative image contribution is important. In Case 3, for example, there is a shift of 3 percent for the wavelength of 10 μm, which at 1 AU (i.e., an Earth diameter of 86 μrad) gives a bias offset of 2.5 μrad if each waveband contributes equally in terms of signal level. These two images are shown in Fig. 8 after first normalizing them to have the same total signal level (with the actual effect dependent on the detector response and the optical throughput). Note that the image on the right (the 10- to 11-μm band) appears to be much more uniform. The intermediate wavelengths will show a continuous behavior in the 5- to 10-μm range.

To determine the center of the Earth, we looked at three approaches: (1) edge detection, (2) centroid determination with bias offset, and (3) maximum-likelihood matching. Ideally there would be a "formula" that would allow for deriving the position of the receiving station without surface feature knowledge, as is needed in the optical wavelengths. Because of the long wavelengths used, 8 to 13 μm, the diffraction pattern limit imparts a significant amount of defocus. For a 30-cm telescope, the airy disk diameter is given by $1.22\lambda/d$, $d = 0.3$, and $\lambda = 8 \times 10^{-6}$ to 13×10^{-6}, so that $1.22\lambda/d \sim 32$ to 52 μrad; assuming optical imperfections, the blurring of a point source can be assumed to be at least 32 to 52 μrad, depending on the wavelength. For a 10-cm telescope, the blurring effect is 3 times larger. The detector pixel size would be chosen differently to meet the Ka-band versus the optical communications requirement. For Ka-band, we will assume a pixel size of 20 to 30 μrad (0.5 to 0.3 pixel accuracy required), and roughly 5 to 10 μrad for optical communications. From Mars, the Earth ranges from 170 μrad at 0.5 AU to 31 μrad at 2.7 AU; the defocus will add 32 to 52 μrad to the image size at the focal plane. The Earth image size at the focal plane will range between 60 and 220 μrad in diameter, with an edge ramp of 16 to 30 μrad.

Table 4 provides the signal estimates at the two prime wave bands, assuming 10 percent combined detector and optics efficiency and a 1-ms integration period through a 30-cm collection aperture. The pixel count is an estimate of the number of available signal pixels at 20:1 and 100:1 signal-to-noise ratios, assuming a 200-electron read noise. Using a 10-μm waveband can increase the signal and pixel count by roughly a factor of 5 with respect to a 5-μm waveband, at the cost of model and system complexity. The image width, including defocus, is limited to the square root of the number of pixels. In the case where there is very large signal available, multi-band operation/detection, using a combination of beam splitters or other optical elements, should be given consideration. Note that for a symmetric point-spread function, the centroid of the image (pre-pixelization) depends only on the image distribution.
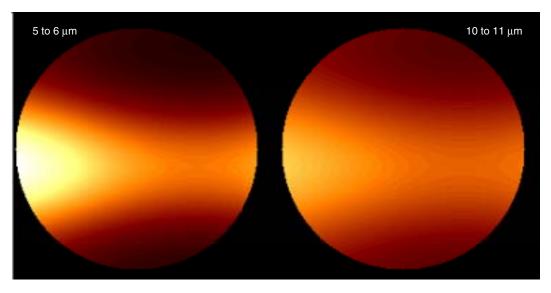

Fig. 8. Earth temperature models from two wavelength bands: 5 to 6 μm and 10 to 11 μm.

1. Edge Detection. Looking at the above simulations (Fig. 8), the sharp dividing line between the edge of a warm planet and cold space seems to be a natural reference. The blackbody model shown in Fig. 8 is somewhat deceiving in that it is only a raw image simulation and does not take into account surface features and the optical/detector effects of the telescope. As stated above, the optics will introduce a ramp at the edge, based on the image and point-spread function. It appears from the models that the entire Earth is usable (as opposed to the lit edge in the visible). The maximum number of edge pixels will be πd, where d is the Earth diameter measured in pixels. For typical edge-detection algorithms, the number of pixels used in the edge calculation will be $E \pi d$, where $E = 4$ or 5. More study is needed, but for a uniform image, an edge-detection accuracy of $\sigma = 0.1$ to 0.2 pixels in the radial direction is reasonable. The minimum and maximum size of the applicable images is still under investigation, and the variation of Earth at the limb is a factor, which is not yet studied in real images.

A d-pixel-diameter image will have a πd pixel edge length; for each axis, the accuracy will range, depending effectively on $\pi d/2$ to $(\pi d/2)^{1/2}$ pixel edge measurements, where the majority of the information for a particular axis comes from edges with intensity gradients with large components in that axial direction. This should end up with an expected rms accuracy of about

$$\frac{\sigma}{(\pi d/2)^{1/2}} \text{ pixel units} \tag{4}$$

Assuming 10 μrad and 30 μrad pixels for optical and Ka-band, respectively, the above estimation gives about 300 nrad and 1200 nrad bias error (1 sigma) with sigma = 0.1 pixel. Bias terms arise because of non-uniformity of the surface emission near the edge of the Earth.

2. Centroid Determination with Bias Offset. Table 6 shows the NEA for the centroiding formula of Eq. (3). Note that the units for sigma are in $1/100$ of a pixel, so that the very first entry is 0.0692 pixels. The main benefit of the center-of-mass centroid algorithm is that the computed NEA does not depend on a model. The drawbacks are that any non-uniformity induces a bias term potentially significantly larger than the optical communications pointing requirements (still acceptable for Ka-band, however) and that the computed NEA depends on the entire image, including pixels providing little positional information, such as those in the center of the uniform image. Bias offset can be done with the Earth models, which gives the offset from the true geometric center of the Earth. This may look like a maximum-likelihood estimate, since the change of the image shape as a function of position appears explicitly.

Table 6. NEA from the center-of-brightness centroiding method.

Total signal electrons per frame	Read noise/ pixel	Image width $N = 5$, $100 \times$ signal (pixels)	Image width $N = 10$, $100 \times$ signal (pixels)	Image width $N = 20$, $100 \times$ signal (pixels)	Image width $N = 30$, $100 \times$ signal (pixels)
25,000	200	6.92	25.38	96.96	214.74
100,000	200	1.79	6.40	24.30	53.74
250,000	200	0.76	2.61	9.76	21.54
500,000	200	0.42	1.34	4.92	10.81
25,000	100	3.58	12.81	48.59	107.48
100,000	100	1.01	3.32	12.26	26.98
250,000	100	0.48	1.41	4.99	10.88
500,000	100	0.30	0.77	2.57	5.51

3. Maximum-Likelihood Matching. The maximum-likelihood estimator approach can be applied to either edges or images; the key feature of either of these approaches requires a model of the Earth's distribution and the noise content. This approach is still under study.

The maximum-likelihood method assumes the existence of a reference thermal image. The uncertainties between the reference image and the received image are modeled as a certain noise model, such as additive white Gaussian disturbances. In order to estimate the x- and y-coordinates of the received image relative to the reference image, two nonlinear equations need to be solved. The optimal solution can be obtained iteratively. From [3], it was shown that standard deviations of 0.031 and 0.016 pixel can be achieved with an average SNR of unity for an image size of 16×16 and 32×32 pixels. A larger image size improves the accuracy.

4. Summary of Bias Error. Table 7 summarizes the achievable bias error for the three investigated centroiding methods. As is shown, all three methods have bias error close to the bias error budget of 100 nrad for optical communications. Depending on the trade-offs in the optics design, such as FOV and telescope size, the requirement can be met. For example, a 5-μrad pixel instead of a 10-μrad pixel gives an 80-nrad bias error with the maximum-likelihood method. Additionally, if the distance becomes 1 AU, the bias error with the edge-detection method will be 118 nrad.

Table 7. Summary of bias error for the three centroiding methods.

Approach	Estimated bias error, nrad	Comments
Edge detection	<300	Assuming a 10-μrad pixel
Centroid determination	Varies	Depends on the image model
Maximum-likelihood matching	<160	Based on a 32×32 image, an SNR of 1

5. Bias Error Sources. The search for a tracking algorithm to achieve sub-microradian pointing in the IR faces a number of challenges. From Mars, the Earth size ranges from 170 μrad in diameter at 0.5 AU to about 34 μrad at 2.5 AU. For a 30-cm telescope, the diffraction limit produces an Airy disk $1.22\lambda/d \sim 32$ to 52 μrad first ring. A 10-cm aperture yields a roughly 100- to 150-μrad-diameter Airy disk. This effect was not evaluated in the above study. Examples of the type of details that need to be considered are listed in Table 8, which assumes 10-μrad pixels, a 1-kHz frame rate, and a 10 percent quantum efficiency (QE).

IV. Summary

A. Is It Feasible?

The analysis in this article shows that the 8- to 13-μm wavelength band can meet optical and Ka-band pointing requirements while the 3- to 5-μm band is not sufficient for optical communication requirements. Certainly, the 3- to 5-μm band can be used for Ka-band with proper parameters, such as aperture size and lower frame update rates. The 3- to 5-μm range can be considered if the detector has a significant advantage in this wavelength regime. Otherwise, the 8- to 13-μm range is more attractive due to (1) the additional available signal and (2) the lower emissivity variation. The obvious advantage over the visible band is the ability to detect the entire perimeter of Earth with low emissivity variation such that the potential centroiding error can be reduced. This solves a major problem that visible image tracking was not able to solve (albedo variation and partially reflected Earth image). Another benefit is a simplified centroiding algorithm due to symmetry of the Earth's shape. This concept is applicable beyond Mars' distance as long as sufficient signal is received. Trade-offs such as larger aperture size and lower detector noise can extend the operating range.

Table 8. Various bias error sources.

Error source	Bias/noise	Comments
Point spread function (PSF)	—	There will be bias if the PSF is asymmetric.
PSF	Noise	Increases image size for 30-cm telescope by at least 50 μrad (depending on whether there is additional defocus). At 2.5 AU, the Earth will be at least $50 + 35 = 85$ μrad in diameter for a 12-μm waveband.
Gravitational bending of light	Bias	Needs to be accounted for to achieve 300 nrad.
Features on surface of Earth, edge effects	Bias	With 10-μrad pixels, the size of the Earth (including defocus) ranges from 8.5 to 22 pixels in diameter, or roughly 580 to 1532 km per pixel. If we attempt to achieve 0.2-μrad bias error, this relates to an Earth ground distance of between 11.6 and 30.6 km.
Perturbations due to interloping objects	Bias, noise	Nearby objects may cause perturbations of the Earth centroid. Assuming a blackbody model, a m_b (bolometric magnitude) magnitude 6 star at 2800 K ($\sim$spectral type M6—red, large amount of signal in the infrared region—roughly a visual magnitude of 10) gives about 3.4×10^6 photons/s, or at 1 kHz, 10% efficiency, 70 electrons per frame/μm between 8 and 12. For a star at the edge of the Earth to cause a perturbation to the 1,000,000-electron Earth signal at 0.67 AU ($\sim$150-μrad diameter), a bias shift of 100 nrad requires about 1300 electrons, or a visual magnitude 6.5 cool star. This is not so likely, but cannot be ignored as an error source. A sun-class star needs to be roughly a visual magnitude 0.5 to cause this type of shift.

B. Characteristics of Infrared Detectors

In order to estimate the NEA under this scenario, a quick survey was performed of available sensors in the appropriate sensitivity bands. Features of various IR detectors are summarized in Table 9. Key parameters of the commercially available IR detectors were obtained and are summarized in Table 10.

Infrared imaging can be accomplished using a variety of sensing technologies that can all be divided conveniently into two groups: namely, cooled and uncooled sensors. A common metric is the noise equivalent temperature difference (NETD). Uncooled (thermal) devices have an NETD on the order of 20 mK. Cooled (photonic) devices have an NETD on the order of 5 mK. The market presently is dominated by cooled sensor products, but the uncooled share of the market is growing rapidly due to the inherent advantages of these products, as outlined below.

The cooled-sensor technologies are principally semiconductor or quantum devices, and they must be cryogenically cooled to operate in the long-wavelength IR region. The equipment required to cool the detectors adds to the complexity, size, and, therefore, cost of the instruments. Maintenance problems and electrical power requirements also become issues for these sensors, as the coolers are mechanical devices incorporating miniature refrigeration units within the camera itself. The major advantages, and the reason for the present popularity of cooled sensors, are that the sensitivity of these cameras can be very high, approaching the theoretical limit for infrared imaging, and they can be used in high-frame-rate applications. The best of these cameras have sensitivities in the 5- to 10-mK (or 0.005 to 0.010 deg C) range, and they can be used in applications requiring the capturing of infrared images at up to one thousand frames per second. A millikelvin, or mK, is a measure of temperature defined as 1/1,000 of a kelvin, which has the same value as a change in 1/1000 of a degree centigrade. Sensitivity in IR imaging

Table 9. Performance and cost of major IR imaging technologies.

Feature	Cooled quantum sensors	Uncooled microbolometers	Uncooled pyrometers	Uncooled microcantilevers
Ultimate sensitivity	3 mK	20 mK	40 mK	3 mK
Response time	Very fast (ns)	Slow (15–29 ms)	Slow (15–20 ms)	Moderate (5–10 ms)
Dynamic range	10^4–10^5	$\sim 10^4$	$\sim 10^3$	$>10^5$
Optics	Large, expensive, f1–f2	Large, expensive, f1–f2	Large, expensive, f1	Small, cheap, f2–f5
Power requirement	High	Low	Low	Low
Ease of fabrication	Difficult	Difficult	Difficult	Standard integrated-circuit (IC) fabrication
Size	Bulky	Moderately small	Moderately small	Small
Camera cost	$50–100K	$20–50K	$7–25K	$5–15K

Table 10. Commercially available IR sensors and their parameters.

Technology	Temperature, K	Wavelength, μm	NEP/NETD, mK	Rate	Resolution	Pixel, μm
VO_2 microbolometer	300	8–12	—	—	128×128	—
VO_x microbolometer	300	—	—	60 Hz / 30 Hz	320×240 / 640×480	51 / 25.4
Si microbolometer	300	7–14	30	60 Hz	320×240	35
Si microbolometer	313	7–14	120	60 Hz	320×256	—
Si microbolometer	300	7–14	—	>60 Hz	320×240	45
$BaSrTiO_3$	300	7.5–13.5	—	60 Hz	330×350	—
SiNx/Al	300	—	—	—	—	—
InGaAs	250	0.9–1.7	—	130 Hz	320×240	40
PbTe on Si	95	3–5	—	—	96×128	75
InSb	77	1–5.4	25	60 Hz	320×256	—
InSb	80	—	—	—	640×512	—
HgCdTe	77	0.9–5	—	80 Hz	1024×1024	18
HgCdTe	77	0.9–5	—	1.5 kHz	128×128	40
QWIP	77	8.0–9.2	50	60 Hz	320×256	—
QWIP (GaAs/AlGaAs)	—	5–15	—	60 Hz	640×486	40
QWIP (GaAs/AlGaAs)	—	6–25	—	—	640×512	24
SiAs IBC	<10	1–28	—	—	512×412	30

applications is defined as the smallest temperature difference between two objects that can be sensed by the camera. The smaller this number, the more sensitive the camera is. These are prime requirements in many military applications and come at a high price.

The primary advantages of the uncooled IR technologies over cooled systems are that uncooled cameras are considerably less expensive, smaller, less power hungry, and more reliable. The driving force in the development of this technology has been the military, actively funding uncooled-sensor technology development for the past two decades. Uncooled IR sensors are fundamentally different from cooled IR sensors in that radiation detection is achieved by measuring the change in total radiant energy absorbed by the sensor. For cooled semiconductor sensor materials, a change in the electrical conduction properties of the material upon absorption of the infrared radiation is measured. The primary technologies in this area include silicon thermoresistive microbolometers, ferroelectric pyrometers, thermoelectric devices, and microcantilever IR sensors. These uncooled technologies are considerably less mature than the cooled IR imaging cameras, with working products having been marketed only since late 1995.

In terms of performance of the commercially available IR detectors, the best detector is a SiAs blocked impurity band (BIB) with a 5- to 30-μm range and a 3×10^{-19} W/$\sqrt{\text{Hz}}$ noise equivalent power (NEP), but it needs to be cooled to <8 K. These detectors have been space qualified, for example in the Space Infrared Telescope Facility (SIRTF). Array sizes from 128×128 to 1024×1024 have been developed. The quantum well infrared photodetector (QWIP) array looks attractive at first glance, but it is actually a narrowband device that can be manufactured over a wide range (narrowband => limited sensitivity). Most other photonic arrays are insensitive beyond 5 μm; 640×320 resolution is common, as well as 30-Hz or 60-Hz operations.

C. Future Work

We have performed a somewhat rigorous analysis to investigate feasibility. Future work can improve this work in terms of refinement so that the available signal and noise can be determined through analysis. Other analysis to be done includes deep-space missions beyond Mars' distance. Implementation and validation of specific algorithms will be the next step. The long-term task includes system integration and test of the communication system with an LWIR camera.

References

[1] J. W. Alexander, S. Lee, and C. Chen, "Pointing and Tracking Concepts for Deep Space Missions," in *Free-Space Laser Communication Technologies XI,* G. S. Mecherle, ed., *Proceedings of the SPIE,* vol. 3615, pp. 230–249, 1999.

[2] H. Tsou and T. Y. Yan, "Maximum-Likelihood Based Extended-Source Spatial Acquisition and Tracking for Planetary Optical Communications," in *Free-Space Laser Communication Technologies XI,* G. S. Mecherle, ed., *Proceedings of the SPIE,* vol. 3615, pp. 214–221, 1999.

[3] T. Y. Yan, "An Extended-Source Spatial Acquisition Process Based on Maximum Likelihood Criterion for Planetary Optical Communications," *Proceedings of the SPIE,* vol. 1635, pp. 273–285, January 1992.

[4] C.-C. Chen, "Effect of Earth Albedo Variation on the Performance of a Spatial Acquisition Subsystem Aboard a Planetary Spacecraft," *The Telecommunications and Data Acquisition Progress Report 42-95, July–September,* Jet Propulsion Laboratory, Pasadena, California, pp. 202–211, November 15, 1988. http://tmo.jpl.nasa.gov/tmo/progress_report/42-95/95T.PDF

[5] W. L. Wolfe and G. J. Zissis, *The Infrared Handbook,* Office of Naval Research, Department of the Navy, pp. 3–30, 5–89, and 5–90, 1978.

[6] C.-C. Chen, E. Hui, and G. Okamoto, "Confidence Range Estimate of Extended Source Imagery Acquisition Algorithms via Computer Simulations," *Free-Space Laser Communication Technologies IV, Proceedings of the SPIE,* vol. 1635, pp. 300–308, 1992.

Appendix

Earth Temperature Model

We begin with a simplified model of the Earth, consisting of a circular disk centered at (0,0), having an average temperature profile based on a cosine function in latitude and a similar cosine function in longitude. The phase of each cosine function also is input to account for seasonal variations in latitude and day–night variations in longitude. The following equation represents the Earth temperature model:

$$E(x,y,MT,la,lo,d,t) = MT + la\cos\left[y\pi - 0.45\cos\left(\frac{(d+155)\,2\pi}{365}\right)\right] - lo\cos\left(\pi\frac{x}{2} + 1.75\pi + t\frac{\pi}{12}\right) \quad \text{(A-1)}$$

where

$$x,y = \text{horizontal and vertical coordinates where the Earth radius } (x^2 + y^2 < 1) \text{ is normalized to 1}$$

$$MT = \text{mean temperature of the Earth in kelvins}$$

$$la = \text{amplitude factor for the latitudinal variation of the Earth's temperature}$$

$$lo = \text{amplitude factor for the longitudinal variation of the Earth's temperature}$$

$$d = \text{day of year}$$

$$t = \text{local time}$$

Keep in mind that the Earth model is stable in time. In other words, sitting above the Earth at any fixed point with respect to the solar system, one is going to see the same image constantly. This model takes the effects of rotation of the Earth into account. The peak temperature generally is found some time in the afternoon as a result of the accumulation of heat at the surface of the Earth. Likewise, the lowest temperature of the day should be found, on average, just before dawn. Figure A-1 is an example plot of the Earth temperature model generated using Eq. (A-1). This is a pretty reasonable looking result. A Southern Hemisphere summer was considered, looking at the Earth from a point that is roughly over the 6 p.m. local time longitude. Hence, the hot afternoon temperature is located to the left side of center, with colder nighttime temperatures to the right. The Northern Hemisphere is in winter, so there is a colder temperature on the upper right-hand side. Total temperatures range from about 320 K (47 deg C) at the hottest to 240 K (−33 deg C) at the coldest.

Using this function, we can define a pixel footprint and integrate in-band power over a desired spectral band, over a desired temperature profile.
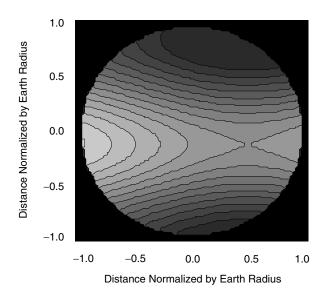
Fig. A-1. Earth temperature model at local time 18:00.